Energetics of Instability Modes in the Cylinder Wake

Z. Y. Ng, T. Vo and G. J. Sheard

The Sheard Lab, Department of Mechanical and Aerospace Engineering
Monash University, Victoria 3800, Australia

Abstract

This study investigates the perturbation kinetic energy budget of the instability modes in the circular cylinder wake using the out-of-plane averaged perturbation kinetic energy (PKE) equation. This equation relates to the instability growth rates predicted through linear stability analysis techniques and provides a means to understand the sources through which the linear modes grow on the two-dimensional base flow. In this study, the linear modes A and B are studied at their corresponding transition Reynolds number. The most dominant rate of production terms contributing to the mode A and B instability growth are those derived from cross-flow gradients of the base flow velocity, although the terms for mode B occur at higher rates than those for mode A. The locus of the regions with high production rates within the flow field (concerning the sum of the two dominant production terms) shows that the perturbations for mode A develop most rapidly in the elliptical core of the forming vortex, while those for mode B are amplified most in the interface between the two forming vortices, reaching a maximum when the vortex sheds from the cylinder. The mode A unstable flow then describes weak secondary regions of production within the elliptical vortex cores further downstream, and is a feature absent in mode B.

Introduction

Flows past cylindrical obstructions have been the subject of keen research interest owing to its ubiquity in nature and engineering, and exhibits fascinating changes in topology which commonly arises from some form of transition in the flow. For the wakes of a circular cylinder immersed in a uniform flow, the time-invariance of the flow is lost through a Hopf bifurcation resulting in the well-known Karman vortex street [10]. Various secondary instabilities then proceed to manifest in the wake such as the mode A and then subsequently mode B which breaks the spanwise-invariance of the flow [19], and the shear layer instability which causes the 'drag crisis' in the cylinder wake [11], amongst others. The readers are directed to a review of the literature by Williamson [20] for more information.

Of interest to this study are the mode A and B instabilities, which form the initial sequence of bifurcations to three-dimensional flow. Linear stability theory applied to these wakes [1] exhibits a strong agreement with the instability modes reported experimentally [18] and later computationally [15]. Utilisation of these linear modes permit further analyses aiming to understand the physical mechanism underlying these transitions. In particular, [8, 16] investigated the extent to which the mode A instability conforms to the elliptical instability mechanism, and hypothesised the hyperbolic mechanism of mode B. Although these transitions have been investigated extensively in the past, the physical genesis of these instabilities are still largely unknown. We approach this problem by viewing the contributions to instability growth through an energetics perspective, which has yet to be applied on cylinder wake flows.

Methodology

The present study expands on several previous works on the stability of the cylinder wake. The flow is governed by the incompressible Navier–Stokes equation

$$\nabla \cdot \boldsymbol{u} = 0,$$
$$\frac{\partial \boldsymbol{u}}{\partial t} + (\boldsymbol{u} \cdot \nabla)\boldsymbol{u} = -\frac{1}{\rho}\nabla p + \nu\nabla^2\boldsymbol{u}. \tag{1}$$

where $\{\boldsymbol{u}, p\}$ are the velocity and pressure fields, and ν and ρ are the kinematic viscosity and density of the fluid. Choosing the characteristic scale for length as the cylinder diameter, d, velocity as the uniform freestream velocity, U_∞, and time as d/U_∞ permits (1) to be characterised by a single parameter, the Reynolds number $Re = U_\infty d/\nu$.

Let $\boldsymbol{Q} = \{\boldsymbol{U}, P\}$ be the solution to the unsteady two-dimensional base flow and $\boldsymbol{q}' = \{\boldsymbol{u}', p'\}$ be an infinitesimal perturbation applied to the base flow such that the total flow $\boldsymbol{q} = \boldsymbol{Q} + \boldsymbol{q}'$. Substituting these into (1) yields the base flow evolution equations which are identical in form to (1), as well as the perturbation evolution equations

$$\nabla \cdot \boldsymbol{u}' = 0,$$
$$\frac{\partial \boldsymbol{u}'}{\partial t} + \mathbf{N}(\boldsymbol{u}) = -\frac{1}{\rho}\nabla p' + \nu\nabla^2\boldsymbol{u}', \tag{2}$$

where $\mathbf{N}(\boldsymbol{u})$ represents the nonlinear advection term

$$\mathbf{N}(\boldsymbol{u}) = (\boldsymbol{U} \cdot \nabla)\boldsymbol{u}' + (\boldsymbol{u}' \cdot \nabla)\boldsymbol{U} + (\boldsymbol{u}' \cdot \nabla)\boldsymbol{u}'.$$

The linearised form of (2) can then be posed as a temporal eigenvalue problem whose analysis can be further simplified by expressing the perturbation field $\boldsymbol{q}'$ by its Fourier integral. Solutions of this form decouples the linearised governing equations for each mode, permitting the stability analysis for each to be performed independently (see [1] for more details).

To arrive at the perturbation kinetic energy (PKE) equation, the scalar product of the perturbation velocity field $\boldsymbol{u}'$ and the momentum equation in (2) is formed, noting that PKE $k' = \boldsymbol{u}' \cdot \boldsymbol{u}'/2$. This equation is defined as (using the index notation and summation convention)

$$\frac{\partial k'}{\partial t} = - U_j\frac{\partial k'}{\partial x_j}$$
$$+ \frac{\partial}{\partial x_j}\left(-\frac{1}{\rho}p'u_i'\delta_{ij} + u_i'u_i'u_j' + 2\nu u_i's_{ij}'\right)$$
$$- u_i'u_j'\frac{\partial U_i}{\partial x_j} - 2\nu s_{ij}'s_{ij}', \tag{3}$$

where $s_{ij}'s_{ij}'$ is the double contraction of the strain-rate tensor s_{ij}'. The spanwise periodicity of the perturbation eigenmode ($\boldsymbol{u}'$) ultimately provides the impetus for one final simplification in that these three-dimensional modes possess a zero out-of-plane average. The out-of-plane (cylinder-spanwise in this system) average of (3) thus simplifies significantly to

$$\frac{\partial \overline{k'}}{\partial t} = -U_j\frac{\partial \overline{k'}}{\partial x_j} - \overline{u_i'u_j'}\frac{\partial U_i}{\partial x_j} - 2\nu\overline{s_{ij}'s_{ij}'}, \tag{4}$$

where the overbars on the various terms denote its out-of-plane average, and perturbation terms $\mathbf{q}'$ now (and hereafter) denote specific eigenmodes. Note that (4) is only valid when it is applied on the linearised modes. In this equation, the first term on the right hand side represents the mean rate of transport of PKE by the baseflow, the second term represents the mean rate of PKE production from base flow gradients, and the last term quantifies the mean rate of PKE dissipation. Since the stability analysis employed predicts the global growth of the perturbations, its growth rate can be related to that of the PKE through

$$\sigma = \frac{1}{2E_k} \int_{\mathcal{V}} \frac{\partial \overline{k'}}{\partial t} \mathrm{d}\mathcal{V}, \qquad (5)$$

where σ is the instability growth rate predicted from the stability analysis, and $E_k = \int_{\mathcal{V}} k' \, \mathrm{d}\mathcal{V}$ is the total PKE. This analysis ultimately provides an insight into the sources feeding the growth or decay of the instability modes. The reader is directed to [13] for more information on the application of this equation. Specifically for the system under investigation, the volume integral of (4) can be fully written out as

$$\frac{\mathrm{d}E_k}{\mathrm{d}t} = \int_{\mathcal{V}} \mathcal{T} + \mathcal{P} + \mathcal{D} \, \mathrm{d}\mathcal{V},$$

where $\mathcal{T}, \mathcal{P}$ and $\mathcal{D}$ are the local PKE transport, production, and dissipation rate terms given by

$$
\begin{aligned}
\mathcal{T} &= -U\frac{\partial \overline{k'}}{\partial x} - V\frac{\partial \overline{k'}}{\partial y}, \\
\mathcal{P} &= -\overline{u'^2}\frac{\partial U}{\partial x} - \overline{u'v'}\frac{\partial U}{\partial y} + \overline{u'v'}\frac{\partial V}{\partial x} - \overline{v'^2}\frac{\partial V}{\partial y}, \\
\mathcal{D} &= -2\nu\overline{s'_{ij}s'_{ij}}. \qquad (6)
\end{aligned}
$$

For brevity, the remainder of this report shall refer to each term in the volume integral equation normalised by E_k as E_{ij}, where $i = \mathcal{T}, \mathcal{P}, \mathcal{D}$ denotes the category of the term, and $j = 1, 2...$ is the term number on the RHS of (6). For example, term $E_{\mathcal{P}2}$ corresponds to the rate term $\int_{\mathcal{V}} -\overline{(u'v'\partial U/\partial y)}/E_k \, \mathrm{d}\mathcal{V}$.

Numerical Method

For all cases, the governing equations are spatially discretised using a nodal spectral-element method, and integrated forward in time using a third-order accurate scheme based on backward differentiation [7, 3]. Here, the flow variables through interconnecting nodes are described through a high order polynomial shape function and interpolated at the Gauss–Legendre–Lobatto quadrature points. The governing equations recast in weak form through the Galerkin method of weighted residuals can then be solved using the quadrature method. The Floquet stability analysis routine also utilises an implicitly restarted Arnoldi method in conjunction with the spectral-element method described above to compute the eigenmodes of the linearised equations. The eigenmodes of the linearised equations necessarily possess perturbations of infinitesimally small magnitudes, and as such its evolution through the linearised form of (2) does not alter the base flow itself. This permits a straightforward computation of the terms directly from a superposition of the phase-linked perturbation field and base flow. The solver has been implemented and validated previously in [14] and [5], in stability analyses of various flows in [12, 17, 9], and in [13] for the PKE analysis.

The mesh adopted for this study replicates that used by [2], but utilises a polynomial shape function of order $N_p = 16$ instead of $N_p = 7$. This increase in resolution was necessary to resolve the perturbations which occur at smaller scales than the base flow.

For the base flow, a no-slip boundary condition was imposed on the cylinder surface, a uniform streamwise velocity for the inlet and transverse boundaries, and a zero reference pressure applied on the outflow boundary. Neumann boundary conditions on the outward normal gradient of pressure were enforced on all boundaries assigned with a Dirichlet velocity condition to preserve the overall third-order accuracy of the time integration scheme [7]. For the evolution of the perturbation field, homogeneous boundary conditions were imposed on all boundaries except for the outflow of the domain where the boundary condition matches that for the baseflow. A comparison of the results

	[1]	[4]	Present
Re_A	188.5	190	188.7
Re_B	259	260.5	258.8
λ_A	3.96	3.97	3.98
λ_B	0.822	0.825	0.824

Table 1: Comparison of the transition Reynolds numbers and critical wavelengths for modes A and B.

obtained from the stability analysis in the present study against several published results (shown in table 1) serves as validation for the mesh and the solver. The remainder of this study concerns itself with the flows near the criticality of each mode in an attempt to investigate the sources through which PKE is derived. For this, the mode A unstable flow was computed at $Re = 189$ and the mode B unstable flow at $Re = 259$ (just above the predicted transition Reynolds numbers), and the corresponding perturbation structures are shown in figure 1. The computations were initialised using base flow solutions at the instant the cylinder experiences maximum lift.
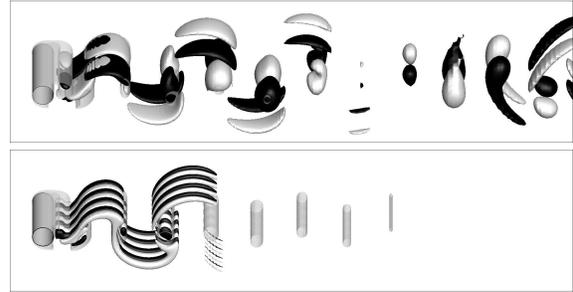

Figure 1: Structure of modes A and B shown to the end of the simulated domain. Light (dark) isosurfaces mark positive (negative) streamwise vorticities at $\pm 0.1 \max |\omega'_x|$, while the translucent isosurfaces describe the vortex loops in the base flow at $\lambda_2 = -1$ [6].

Results and Discussions

Figure 2 illustrates the contribution of each term in the total (volume integrated) PKE equation over the shedding cycle. For mode A, each term acts to distinctly increase or subtract from the instability growth rate throughout the shedding cycle (does not change sign). The dominant positive contribution rate terms for this mode are $E_{\mathcal{P}2}$ and $E_{\mathcal{P}4}$, while the instability growth is most significantly damped through the dissipation term $E_{\mathcal{D}1}$ as anticipated. The profile for mode B instead shows that the contribution of terms $E_{\mathcal{P}1}$ and $E_{\mathcal{P}3}$ to the instability growth switches between phases of promoting and impeding the instability growth, albeit at negligible amplitudes. Similar to mode A, the dominant terms through which perturbation growth accelerates are the $E_{\mathcal{P}2}$ and $E_{\mathcal{P}4}$ terms, and is most dissipative through $E_{\mathcal{D}1}$. Although both modes derive perturbation growth

predominantly through similar terms, the distribution of most terms for mode B appear to reach a peak at similar times, suggesting that a common event in the base flow instigates the instability. The instantaneous values of the transport terms for mode B are approximately related through $E_{T1} = -E_{T2}$. Overall, the contribution terms for mode A excite the flow at lower rates than those for mode B, with mode A terms generally fluctuating up to a rate of approximately $E_{ij} \approx 0.2$ in contrast to those for mode B with positive rate terms of up to $E_{ij} \approx 0.6$ and dissipation events up to $E_{ij} \approx 1$. We next considered the
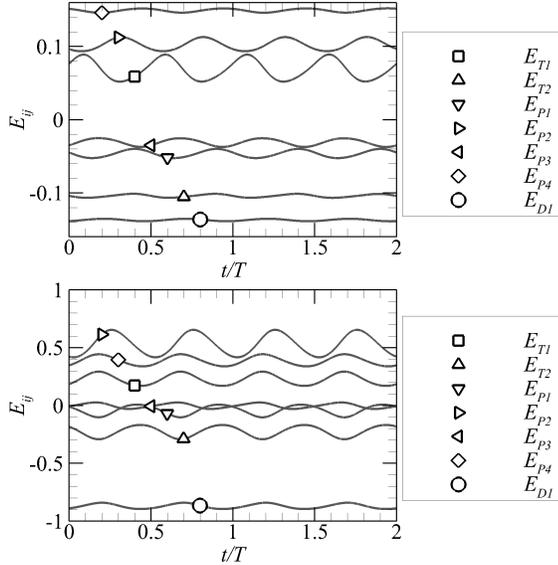

Figure 2: Distribution of E_{ij} over the shedding period for modes A (top) and B (bottom).

period averages of E_{ij} to determine the mean rate at which each term effects perturbation growth. These results are shown in figure 3, and are presented as a percentage of the net period-averaged production rate $\left(\Sigma \overline{E_{\mathcal{P}}} \right)$. An interesting feature of this result is that the dissipation of total PKE for mode B occurs at $\approx 100\% \Sigma \overline{E_{\mathcal{P}}}$—these cases being computed close to criticality of the modes lead to $\overline{dE_k / dt} \approx 0$, and because both transport terms negate each other for mode B, the total production rate necessarily balances the dissipation rate. This effect can be observed in the eigenmode in figure 1 wherein the perturbation structures for mode B fully dissipate within several shedding cycles before reaching the end of the computed domain. A similar argument applied to the energetics of mode A then relates the perturbation structures observed at the outflow boundary to an insufficient dissipation rate relative to the total production rate. Another benefit of this analysis is the ability to visualise
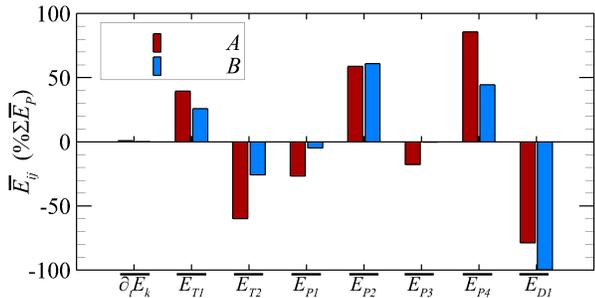

Figure 3: Period-averages of E_{ij} displayed as a percentage of net total PKE production ($\Sigma E_{\mathcal{P}}$).

the spatial distribution of these terms contributing to the growth rate of the instability as shown in figure 4. The top row in the figure corresponds to the local rate of instability growth $\partial_t k'$ obtained from the sum of the terms, the middle row of the figure corresponds to the sum of the production terms $\Sigma \mathcal{P}$, and the bottom row corresponds to the sum of the two terms contributing most aggressively to the instability growth ($\mathcal{P}2 + \mathcal{P}4$). For both modes, high PKE growth rates are observed to occur within the strained 'tails' of the shedding vortex, and in the case of mode B, in a secondary region along the interface where the forming vortices interact. Observation of the net PKE production rate as well as the dominant production rate terms describe regions where the instability growth is most aggressive. These regions possess a high PKE production rate, and for mode A are observed to originate in the core of the forming vortices, intensifying within the elliptic core region as the vortex develops. These regions then move into the 'tails' of the shedding vortex, amplified primarily by a high strain rate. These PKE production maxima then diminishes rapidly with the strained vortex tails after the vortex is shed as it relaxes back into an elliptical form. Weak secondary regions of PKE production are observed to develop within the cores of the elliptical vortices by about $x \approx 10d$, but decays as it advects downstream. The description of the path and movement of these high production rate regions for mode A reproduces almost exactly the description of the co-operative elliptical instability mechanism proposed by [16], but through an energetics perspective. For mode B, a similar re-
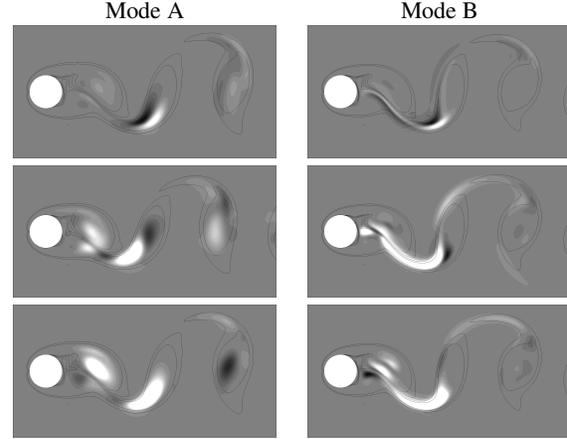
Mode A	Mode B

Figure 4: Distribution of (top) $\partial_t k'$, (middle) $\Sigma \mathcal{P}$, and (bottom) $\mathcal{P}2 + \mathcal{P}4$ for (left) mode A, and (right) mode B. Dark(light) contours indicate regions of negative(positive) growth rate contribution.

gion of high PKE production rate is again observed to initially develop within the elliptical core region of the forming vortex. However, the counter-rotating vortices in the forming region are observed to interact at an earlier phase of the vortex shedding, causing a secondary PKE production region to develop rapidly along the interface between the forming vortices, which dominates over the growth within the elliptical core. This production region amplifies strongly within the braid region between the primary vortices. As the vortex is shed, the production region is observed to extend in into the forming region of the wake, providing a continuity in perturbation production which possibly acts as a 'blueprint' for the perturbation growth and causing the symmetry observed for mode B [21]; the production regions for mode A within these braid shear layers appear to be separated by a small region of perturbation decay which breaks up the feedback. Again, these production regions for mode B dissipate rapidly after the vortex is shed as it relaxes back into an elliptical shape. Unlike mode A, the elliptical vortices downstream do

not show any propensity for a further elliptical instability. For both modes A and B, these production regions are observed to develop most intensely within the first shedding cycle.

Conclusions

The sources contributing to perturbation kinetic energy growth are elucidated for the mode A and B instabilities in the cylinder wake. For mode A, a net negative rate is observed for the transport terms, justifying the net outflow of the perturbations observed in the eigenmode; the corresponding terms for mode B sum to zero, reflecting the containment of the disturbance structure within the domain. For the production terms, mode A is observed to derive PKE at a significantly lower rate ($E_{ij} \approx 0.2$ for the largest positively contributing term) compared to mode B, whose largest positive contributor fluctuates at $E_{ij} \approx 0.5$. Of the four production terms, only the terms involving cross-flow gradients of base flow velocity ($E_{\mathcal{P}2}$ and $E_{\mathcal{P}4}$ in this report) are significant, with the streamwise gradient production terms $E_{\mathcal{P}1}$ and $E_{\mathcal{P}3}$ being either weakly dissipative as observed for mode A, or negligible as observed for mode B.

For the local distribution of each term, the path followed by the the high production region in mode A follows a similar description for the perturbation growth described for the cooperative elliptical instability mechanism in [16]—perturbation growth originates in the elliptical core of the forming vortex and is stretched out into the tail of the vortex as it sheds, becoming amplified by an increased local strain rate. A different scenario is observed for mode B where the PKE growth is strongly amplified along the stagnation streamline to the shedding vortex. In both cases, the largest contribution to PKE growth is observed to occur as the vortex splits to form the hyperbolic points.

Acknowledgements

References

[1] Barkley, D. and Henderson, R. D., Three-dimensional Floquet stability analysis of the wake of a circular cylinder, *J. Fluid Mech.*, **322**, 1996, 215–241.

[2] Blackburn, H. M. and Lopez, J. M., On three-dimensional quasiperiodic Floquet instabilities of two-dimensional bluff body wakes, *Phys. Fluids*, **15**, 2003, L57–L60.

[3] Blackburn, H. M. and Sherwin, S. J., Formulation of a Galerkin spectral element-Fourier method for three-dimensional incompressible flows in cylindrical geometries, *J. Comput. Phys.*, **197**, 2004, 759–778.

[4] Carmo, B. S., Sherwin, S. J., Bearman, P. W. and Willden, R. H. J., Wake transition in the flow around two circular cylinders in staggered arrangements, *J. Fluid Mech.*, **597**, 2008, 1–29.

[5] Hamid, A. H. A., Hussam, W. K. and Sheard, G. J., Combining an obstacle and elecrically driven vortices to enhance heat transfer in a quasi-two-dimensional mhd duct flow, *J. Fluid Mech.*, **792**, 2016, 364–396.

[6] Jeong, J. and Hussain, F., On the identification of a vortex, *J. Fluid Mech.*, **285**, 1995, 69–94.

[7] Karniadakis, G. E., Israeli, M. and Orszag, S. A., High-order splitting methods for the incompressible Navier–Stokes equations, *J. Comput. Phys.*, **97**, 1991, 414–443.

[8] Leweke, T. and Williamson, C. H. K., Three-dimensional instabilities in wake transition, **17**, 1998, 571–586.

[9] Ng, Z. Y., Vo, T. and Sheard, G. J., Stability of the wakes of cylinders with triangular cross-sections, *J. Fluid Mech.*, **844**, 2018, 721–745.

[10] Provansal, M., Mathis, C. and Boyer, L., Bénard-von Kármán instability: transient and forced regimes, *J. Fluid Mech.*, **182**, 1987, 1–22.

[11] Roshko, A., Perspectives on bluff body aerodynamics, *J. Wind Eng. Ind. Aerod.*, **49**, 1993, 79–100.

[12] Sheard, G. J., Fitzgerald, M. J. and Ryan, K., Cylinders with square cross-section: wake instabilities with incidence angle variation, *J. Fluid Mech.*, **630**, 2009, 43–69.

[13] Sheard, G. J., Hussam, W. K. and Tsai, T., Linear stability and energetics of rotating radial horizontal convection, *J. Fluid Mech.*, **795**, 2016, 1–35.

[14] Sheard, G. J., Leweke, T., Thompson, M. C. and Hourigan, K., Flow around an impulsively arrested circular cylinder, *Phys. Fluids*, **19**, 2007, 083601.

[15] Thompson, M., Hourigan, K. and Sheridan, J., Three-dimensional instabilities in the wake of a circular cylinder, *Exp. Therm. Fluid Sci.*, **12**, 1996, 190–196.

[16] Thompson, M. C., Leweke, T. and Williamson, C. H. K., The physical mechanism of transition in bluff body wakes, *J. Fluids Struct.*, **15**, 2001, 607–616.

[17] Vo, T., Montabone, L. and Sheard, G. J., Linear stability analysis of a shear layer induced by differential coaxial rotation within a cylindrical enclosure, *J. Fluid Mech.*, **738**, 2014, 299–334.

[18] Williamson, C. H. K., The existence of two stages in the transition to three-dimensionality of a cylinder wake, *Phys. Fluids*, **31**, 1988, 3165–3168.

[19] Williamson, C. H. K., Three-dimensional wake transition, *J. Fluid Mech.*, **328**, 1996, 345–407.

[20] Williamson, C. H. K., Vortex dynamics in the cylinder wake, *Annu. Rev. Fluid Mech.*, **28**, 1996, 477–539.

[21] Yildirim, I., Rindt, C. C. M. and van Steenhoven, A. A., Mode C flow transition behind a circular cylinder with a near-wake wire disturbance, *J. Fluid Mech.*, **727**, 2013, 30–55.